Journal of the European Ceramic Society **16** (1996) 1365–1375

PII: S0955-2219(96)00057-X
0955-2219/96/$15.00

Controlled Wet Erosive Wear of Polycrystalline Alumina

A. Franco & S. G. Roberts*

Department of Materials, University of Oxford, Oxford OX1 3PH, UK

(Received 10 January 1996; revised version received 14 February 1996; accepted 28 February 1996)

Abstract

Controlled wet erosive wear tests were performed on polycrystalline alumina specimens of mean grain size G = *1·2, 3·8 and 14·1 μm and on sapphire specimens. The tests were performed by using an apparatus consisting of a jet body that rotates immersed in the slurry medium (SiC grits). Impacts are normal to the target surface. The construction and calibration of the apparatus are described. The impacting velocity used was 2·7 m* s^{-1}. *The weight loss of polycrystalline alumina and sapphire specimens increased linearly with impacting time. The wear rate of polycrystalline alumina specimens increased with grain size. Wear rates of 1·83, 8·36 and 11·3 nm* s^{-1} *correspond to* G = *1·2, 3·8 and 14·1 μm, respectively. For sapphire specimens the wear rate was 9·56 nm* s^{-1}. *Worn surfaces of both polycrystalline alumina and sapphire specimens were analysed by scanning electron microscopy. © 1996 Elsevier Science Limited*

1 Introduction

It is well known that the wear resistance of polycrystalline alumina materials has a strong dependence on grain size. For example, in wear due to sliding,[1–5] grinding,[5,6] sawing,[7] dry erosion[8] and wet erosion,[9] the wear rate increases with the grain size.

In the study of wet erosive wear of a series of polycrystalline alumina specimens reported by Miranda-Martinez *et al.*,[9] the tests were conducted using an apparatus where the specimens were discs clamped between blocks of polyurethane in a central shaft that rotates immersed in a pot filled with slurry. Approximately 50% of the disc area was exposed to impacts. The most worn area was the lower part (bottom) of the exposed area. Using this tester, it is quite difficult to control some important parameters, such as impact velocity, impact angle and the number of impacting particles per unit of time.

Several other types of wear tester have been used to study the mechanisms and rates of erosion produced by single and multiple particle impacts, carried by either wet or dry media, on brittle materials.[10–20] None of these machines is suitable for the study of the early stages or basic mechanisms of surface damage, because even for a very short test time the amount of material removed is large and the control of impacting angle is quite difficult.

Here we report the design and use of a new slurry wear tester. Controlled particle impacts are produced normal to the test surface. The velocity of impacting particles was determined by comparing the crater depths produced by particle impacts and hardness indentation. Normal particle impact tests were performed on polycrystalline alumina and sapphire specimens using SiC grits in water as the eroding medium. In order to observe the evolution and mechanisms of surface damage in the early stages of wear on a polished surface, tests were performed for 1 and 15 min. To measure the weight loss and wear rate, tests were of 660 min duration.

2 Wear Machine — Construction and Calibration

2.1 Description

The rotating jet slurry wear tester is shown schematically in Fig. 1. It consists basically of three parts: (1) an electric motor, (2) a jet body–sample holder and (3) a slurry pot. The motor operates at nominal rotating speeds ranging from 10 to 200 rev min^{-1}. The jet body–sample holder is mounted on one end of a 275 mm stainless steel arm attached to a stainless steel shaft connected to the motor. At the other end of the arm a stainless steel paddle is attached to mix the slurry. Both the jet body and the paddle rotate in a groove delimited by the pot's inner wall and a fibreglass cylinder in

*To whom correspondence should be addressed.

the centre of the pot. The groove width is 65 mm and the jet body rotates 20 mm from the bottom of the pot in the groove. A buffer system is mounted 3 mm above the rotating arm in order to prevent the slurry from rotating with the jet body. The buffer system consists of eight stainless steel blades. The pot is placed on a table and attached to a mechanical jack to control its position in

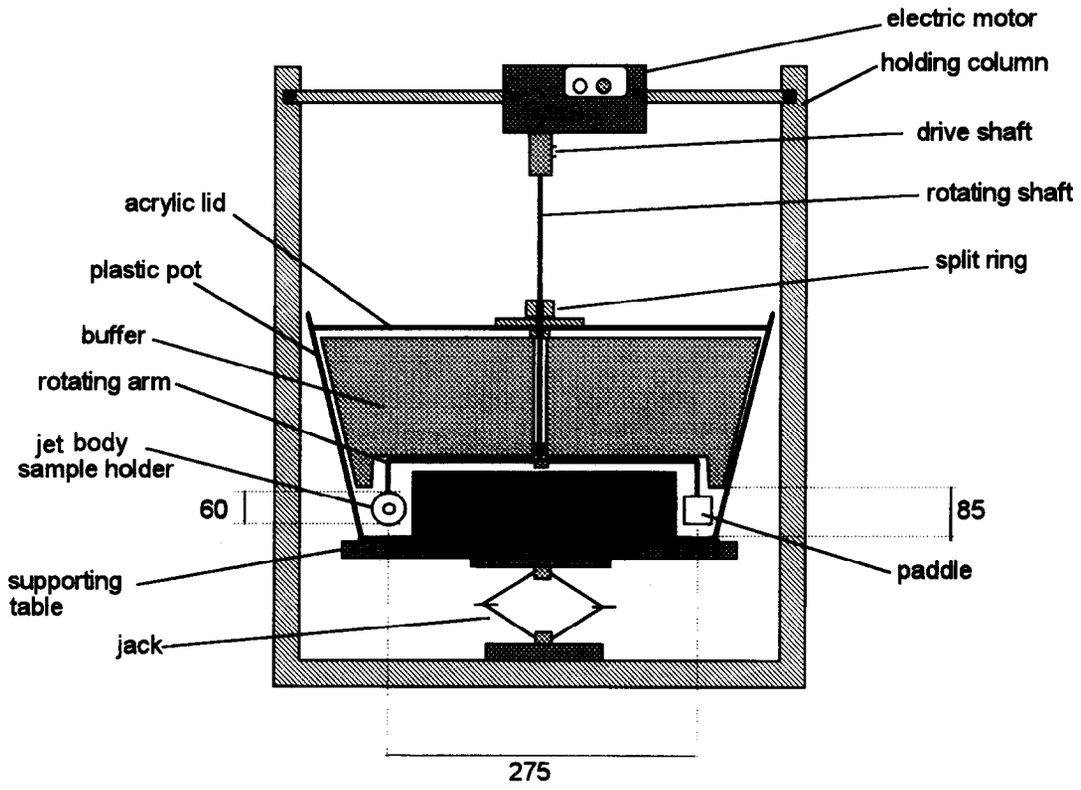

Fig. 1. Schematic diagram of the wear test machine. The machine consists of three parts: a motor, rotating jet body and slurry pot. Dimensions are in mm.

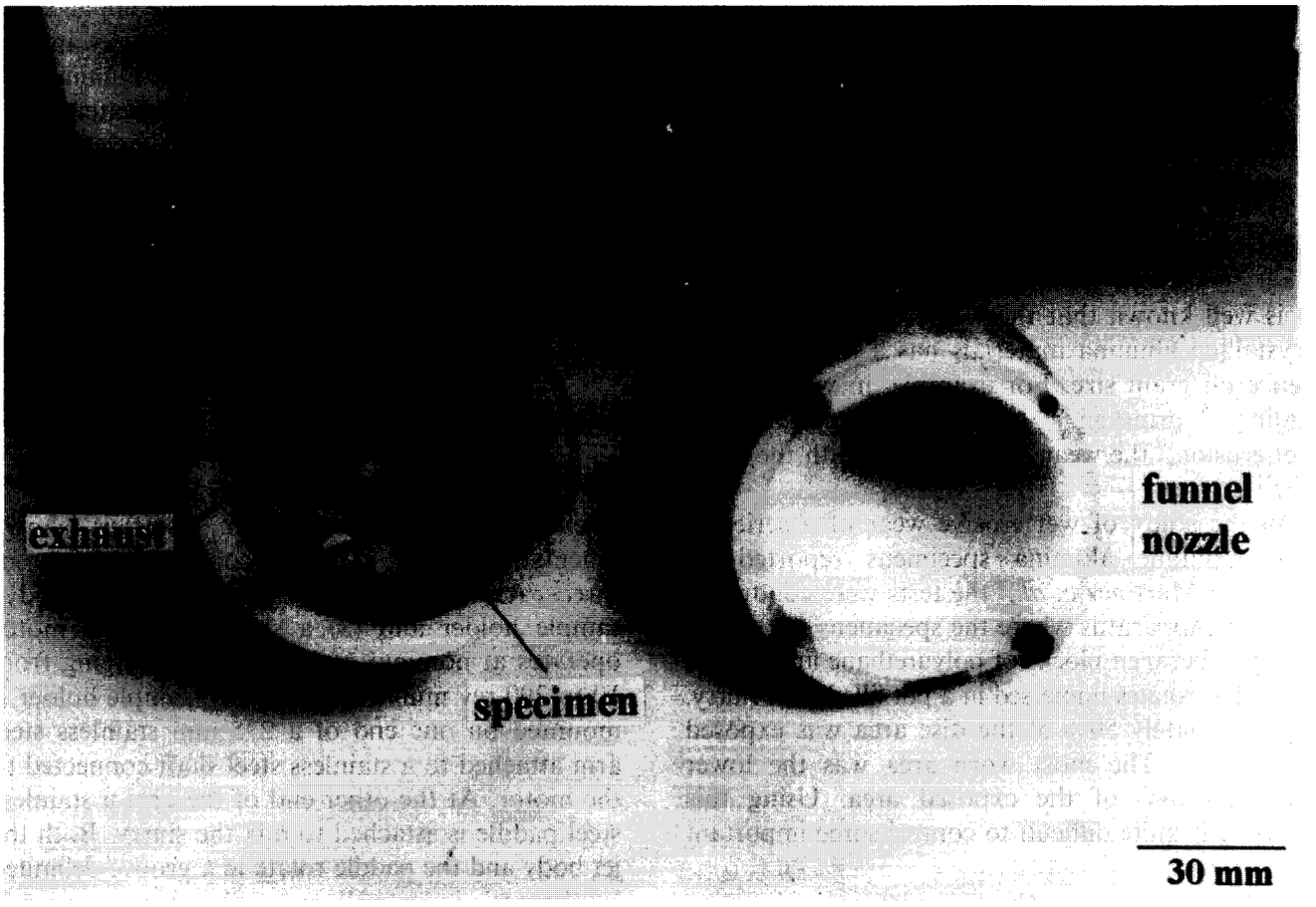

Fig. 2. The jet body–sample holder, showing the sample holder, slurry exhaust and funnel–nozzle system.

relation to the rotating arm. The jack also is used to lower and lift the pot during specimen and slurry changes.

The jet body–sample holder is made of nylon and consists of a funnel–nozzle and a lid as shown in Fig. 2. The diameters of funnel mouth and nozzle are 50 and 5 mm, respectively. The ratio of 10 between the funnel mouth and nozzle is responsible for accelerating the slurry when the jet body rotates. The sample holder is a nylon disc (40 mm diameter) placed in the bottom of the lid.

2.2 Calibration

2.2.1 Theoretical consideration—impact velocity

When a jet body rotates at a frequency f in a fluid, its linear velocity v_f can be calculated by

$$v_f = 2\pi r_a f \tag{1}$$

where r_a is the rotating arm length. If the jet body is a funnel–nozzle system, the velocity at which the fluid flows into the funnel is the same as the velocity v_f of the jet body. Hence, the velocity of the fluid at the nozzle v_n is given by

$$v_n = 2\pi\left(\frac{r_f}{r_n}\right)^2 r_a v \tag{2}$$

where r_f and r_n are the radii of the funnel and nozzle cross-section areas, respectively.

If a spherical particle strikes a metal surface, at low speed, producing plastic deformation, the crater size and maximum penetration should be a function solely of the normal kinetic energy during the impact. According to Hutchings,[21] approximately 90% of the particle's kinetic energy, during normal impacts on soft metals, is dissipated in plastic deformation (~80% heat and ~10% stored energy) and 10% is used in rebound velocity. The dissipated energy due to plastic deformation is given by

$$K_{imp} = \frac{1}{2}m(v_{imp}^2 - v_r^2) = \frac{1}{2}mv_{imp}^2(1 - e^2) \tag{3}$$

where m is the mass of particle, v_{imp} is the normal impact velocity, e is the coefficient of restitution (v_r/v_{imp}) and v_r is the normal rebound velocity. The fraction of the kinetic energy at impacts that is dissipated in plastic deformation is given by $(1 - e^2)$, and e varies with impact velocity as shown by Kosel *et al.*[22] On the other hand, if the same sphere is slowly loaded onto the same soft surface, the work done by the load to produce plastic deformation (plastic work) during indentation (of depth h_{max}) is given by

$$W = \int_0^{h_{max}} P\mathrm{d}h = Ph_{max} \tag{4}$$

where P is the indentation load and h_{max} is the maximum penetration of the spherical indenter (indentation depth).

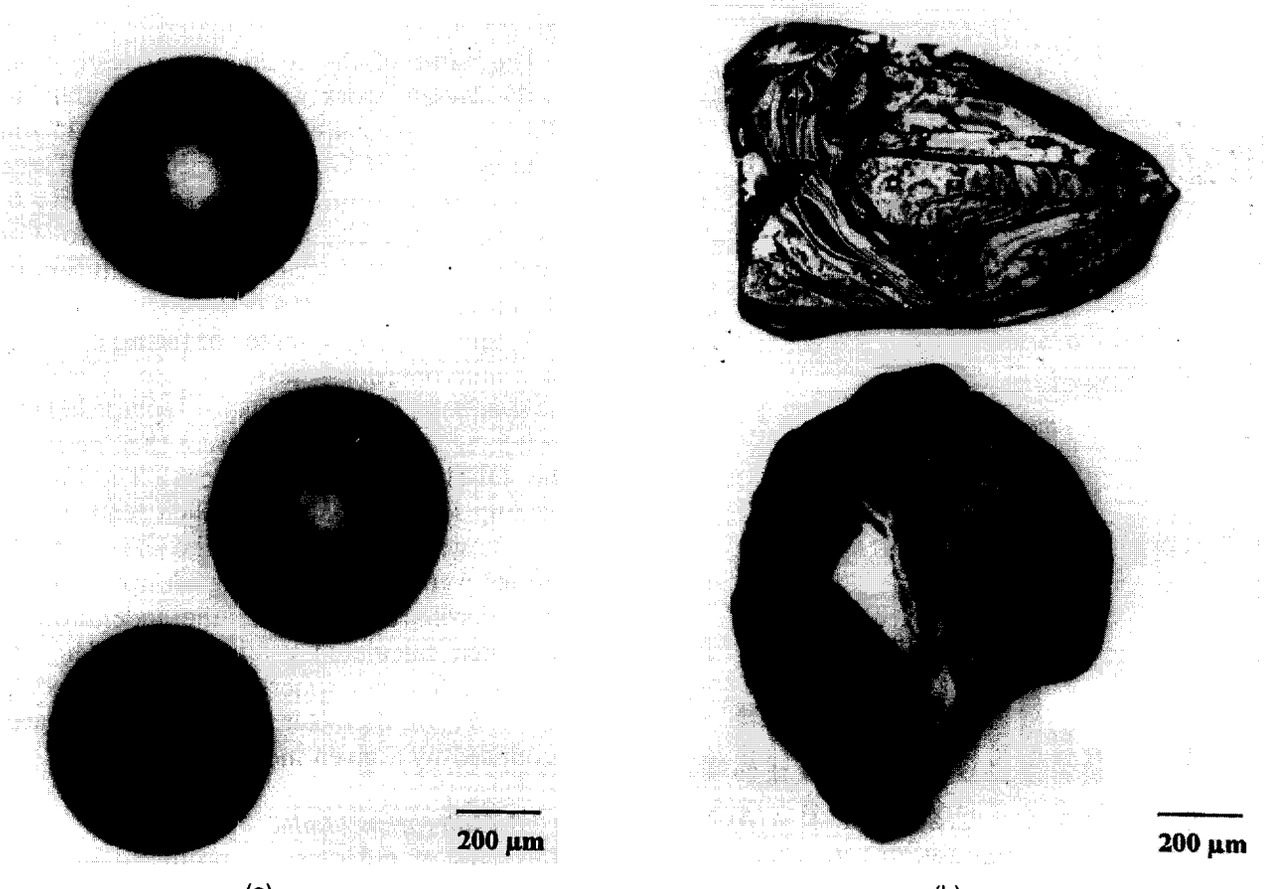

(a) (b)

Fig. 3. Optical micrographs of (a) ballotini (lead glass beads) and (b) SiC grits.

Assuming that the response of soft materials to plastic deformation is independent of strain rate[21–24] so that the depths of the craters produced by single particle impacts and slow load indentation are the same, the velocity of single particle impacts can be calculated by combining eqns (3) and (4).

$$v_{imp} = \left[\frac{2Ph_{max}}{m(1-e^2)}\right]^{1/2} \quad (5)$$

where P is the applied load to produce an indentation of the same size as the single particle impact crater of depth h_{max}.

The depth, h_{max} can be calculated by Pythagoras' theorem:

$$h_{max} = R - (R^2 - r^2)^{1/2} \quad (6)$$

where R is the radius of the spherical indenter and r is the radius of the crater produced either by single particle impact or slow load indentation.

2.2.2 Measurement method — impacting velocity

The velocity of normal particle impacts in this apparatus was calculated by measuring the crater depth produced by single particle impacts onto soft metal and using the energy balance model.

Lead glass beads (ballotini), provided by Jencons Scientific Limited, Leighton Buzzard, UK [Fig. 3(a)], were used as impacting particles and OFHC copper as the target material. The rotating speed f of the jet body immersed in the slurry was measured using a tachometer. Table 1 shows the values of v_f and v_n for each rotating speed f.

Table 1. Jet body rotating speed (f), and velocity of the fluid at the funnel entrance (v_f) and at the nozzle exit (v_n)

Jet body rotating speed f (*rev min*$^{-1}$)	v_f (*m s*$^{-1}$) [*eqn (1)*]	v_n (*m s*$^{-1}$) [*eqn (2)*]
60	0·63	13·29
80	0·84	17·73
100	1·04	22·16
120	1·26	26·59
140	1·47	31·02
160	1·67	35·45
180	1·88	39·88
200	2·10	44·32

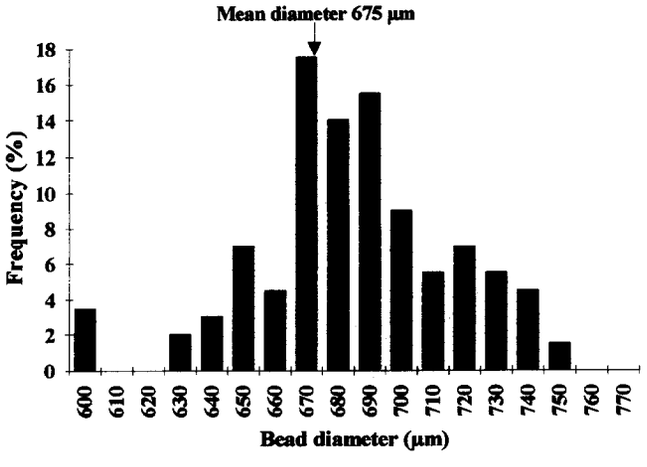

Fig. 4. Size distribution of 200 ballotini. The mean diameter is 675 μm.

A histogram of the diameter of 200 ballotini, measured using a micrometer, is shown in Fig. 4. The average diameter is 675 μm. The average weight of a ballotino was determined (by weighing 600 beads) as $5{\cdot}625 \times 10^{-4}$ g. OFHC copper bars of 2 × 3 × 3 mm were cut, annealed at 300°C for 1 h, mechanically ground with 1 μm alumina slurry and polished on 14, 6 and 1 μm diamond-paste impregnated cloths. To obtain strain-free and highly reflecting surfaces, the specimens were electropolished for 15 min, at 1·8 V DC, using a copper cathode, in a solution of 700 ml of orthophosphoric acid and 300 ml of distilled water.

The copper bars were mounted in the jet body system. The specimen surface was positioned at 3 mm from the end of the nozzle, facing normal to its centre. The slurry consisted of 1 kg of ballotini dispersed in 8 litres of water. Each test was performed for a time of 15 s, chosen so as to make it possible to measure crater diameters by giving a sufficient number of craters produced by single particle impacts without a large number of craters overlapping. Two rotating jet body speeds (140 and 180 rev min^{-1}) were tested. For each speed, 30 isolated craters were measured and the corresponding crater depths were calculated by using eqn (6).

The value of the coefficient of restitution used in the present work was the same as that used by Clark[25] and measured by Kosel[26] for 635 μm steel spheres on OFHC copper specimens. The coefficient of restitution decreases from 0·43 to 0·30 as the impact velocity increases from 5 to 27 m s^{-1}. The value for the coefficient of restitution used in all our calculations was 0·36.

A ballotino was mounted in the tip of an indenter of a microhardness tester (model MHT-1, Matsuzawa Seiki Co. Ltd, Tokyo, Japan). Indentations of 0·5, 1, 2, 3, 5 and 10 N were then performed on the OFHC copper specimens. The indentation holding time was 5 s. For each load a set of 20 indents was performed and the sizes of the indentations were measured using an optical system on the microhardness tester; the indentation depth was then calculated using eqn (6). The test was repeated for two spherical steel indenters of 500 and 1000 μm diameter to compare the crater sizes produced by a given indentation load.

2.2.3 Calibration results

The sizes of indentations produced by slow load indentation on OFHC specimens are shown in Fig. 5. In this plot there are three curves which

correspond to the indentation depth produced by spherical indenters of mean diameters 500, 675 and 1000 μm. The depth increases linearly with the applied load and, for a given load, the indentation depth decreases as the indenter diameter increases.

A best-fit polynomial regression of first order for the indentation depth versus load curve produced by the 675 μm ballotino indenter is given by the following equation

$$h_{imp} = (0{\cdot}10756 + 0{\cdot}62157\,P) \times 10^{-6} \quad (7)$$

where P is the applied load to produce plastic deformation of depth h_{imp}. Inserting the above equation into eqn (5), the particle impact velocity (v_{imp}) can be determined by measuring the depth of craters produced by impacts h_{imp} as

$$v_{imp} = \left[\frac{2}{m(1-e^2)}\left(\frac{h_{imp} - 0{\cdot}10756 \times 10^{-6}}{0{\cdot}62158 \times 10^{-6}}\right)h_{imp}\right]^{1/2} \quad (8)$$

Figure 6 shows the distribution of crater depths produced by single ballotino impacts. In Fig. 6 (a) (140 rev min^{-1}), crater depths range from 0·11 to 0·45 μm; in Fig. 6(b) (180 rev min^{-1}), crater depths range from 0·78 to 1·61 μm. This scatter in crater depth can be attributed to:

(1) The ballotini used as impacting particles showed a scatter in size, as shown in Fig. 3; and
(2) fluid turbulence causes particles to collide with each other and with the nozzle wall, which decelerates them and changes their trajectory before striking the target. Some researchers[27,28] attributed some deceleration to the formation of a thin layer of water between the particles and the target during impacts.

Impact velocities were calculated using the most frequent crater depths (Fig. 6), the average mass of the impacting particle, (5·625 $\times$ 10^{-4} g) and the coefficient of restitution (0·36) in eqn (8); the results are shown in Table 2. For a rotating speed of 140 rev min^{-1} the impact velocities range from 0·28 to 0·52 m s^{-1}. For a jet body rotating speed of 180 rev min^{-1} the impact velocities range from 1·78 to 2·96 m s^{-1}.

Figure 7(a) shows a micrograph of indentations produced by slow loads (5 s holding time) of 0·5, 1, 2, 3, 5 and 10 N, using a ballotino indenter, while Fig. 7(b) shows a micrograph of craters produced by single ballotino impacts onto an OFHC copper specimen at 180 rev min^{-1}. Typical impact crater dimensions of 0·815 and 1·26 μm diameter correspond in size to indentations made with 1 and 2 N loads, respectively.

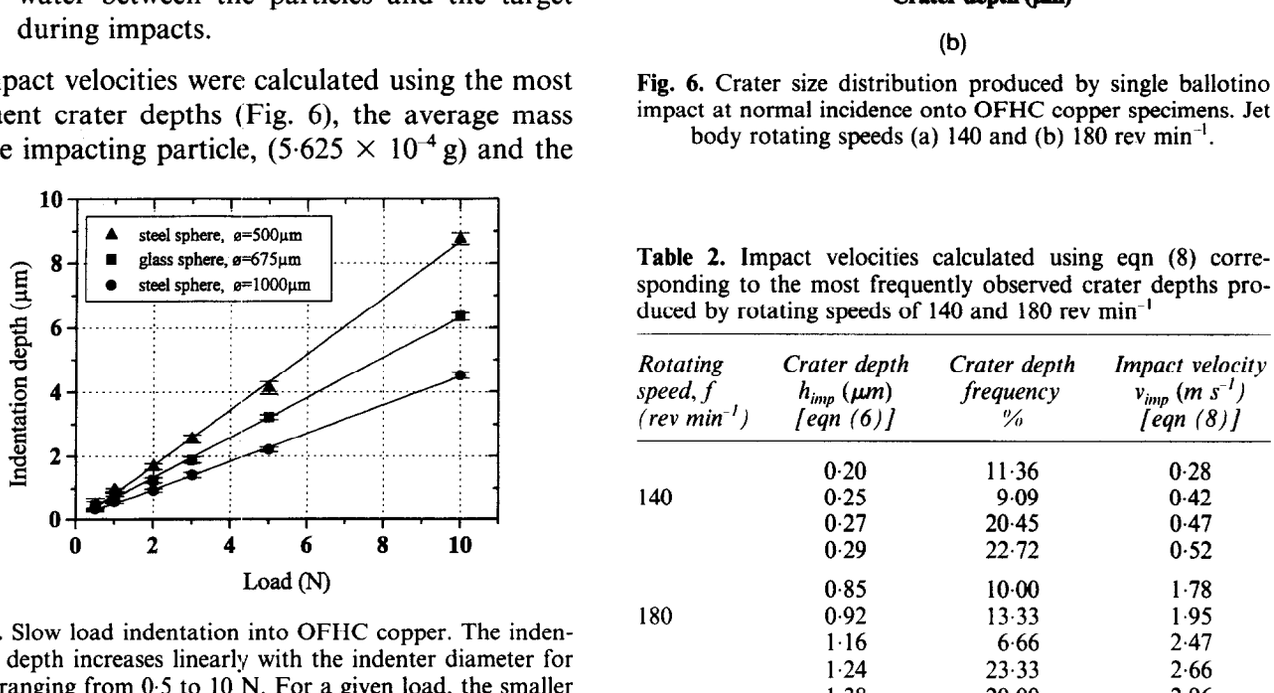

Fig. 6. Crater size distribution produced by single ballotino impact at normal incidence onto OFHC copper specimens. Jet body rotating speeds (a) 140 and (b) 180 rev min^{-1}.

Fig. 5. Slow load indentation into OFHC copper. The indentation depth increases linearly with the indenter diameter for loads ranging from 0·5 to 10 N. For a given load, the smaller the indenter, the deeper the crater produced.

Table 2. Impact velocities calculated using eqn (8) corresponding to the most frequently observed crater depths produced by rotating speeds of 140 and 180 rev min^{-1}

Rotating speed, f (rev min^{-1})	*Crater depth h_{imp} (μm) [eqn (6)]*	*Crater depth frequency %*	*Impact velocity v_{imp} (m s^{-1}) [eqn (8)]*
140	0·20	11·36	0·28
	0·25	9·09	0·42
	0·27	20·45	0·47
	0·29	22·72	0·52
180	0·85	10·00	1·78
	0·92	13·33	1·95
	1·16	6·66	2·47
	1·24	23·33	2·66
	1·38	20·00	2·96

3 Wet Erosive Wear Tests on Polycrystalline Alumina and Sapphire Specimens

3.1 Sample fabrication

Polycrystalline alumina materials were fabricated using high purity, (99·9%) α-Al_2O_3 powder (Sumitomo AKP-50, Japan) of mean particle size ~180 nm. Alumina specimens of mean grain size G = 1·2 μm (referred to later as F) were produced by hot-pressing the powder in a 25 mm diameter graphite die at 20 MPa and 1300°C for 30 min. Specimens of grain size 3·8 and 14·1 μm (referred to later as M and C, respectively) were produced by pressureless-sintering, in air, of powder discs 37 mm diameter that had been uniaxially pressed at 50 MPa in a stainless steel die then cold-isostatically pressed at 300 MPa. The sintering conditions and characteristics of the hot-pressed alumina specimens are shown in Table 3.

3.2 Wet erosive wear tests

The specimens were cut into bars of dimensions 9 × 4 × 4 mm, mechanically ground with 14 μm SiC slurry, polished on cloths impregnated with 6 μm polycrystalline diamond and finished with a 'Syton' polish. The tests were done in a slurry medium of 1·5 kg of SiC grits with a mean size of ~780 μm and a mean mass of 9·10 × 10^{-4} g, dispersed in 8 litres of water. SiC grits (specified as 24 C6) were provided by Washington Mills, Electro Mineral Ltd, Manchester, UK. [Fig. 3(b)]. The jet body rotating speed was 180 rev min^{-1}. Assuming that the 780 μm diameter SiC grit particles travel at the same velocity as 675 μm ballotini under the same fluid flow conditions, the impact velocity is most likely to be 2·7 ± 0·4 m s^{-1} (Table 2).

Tests were performed for different periods, 1 and 15 min, to observe the mechanisms and evolution of surface damage, and for 660 min to measure the weight loss of each specimen. The wear rate, R, was calculated as:

Table 3. Sintering and hot-pressing conditions and characteristics of polycrystalline alumina specimens

Material	*Sintering condition*		*Bulk density* ($g\ cm^{-3}$)	*Mean grain size* (μm)
	Temp. (°C)	*Holding time* (*h*)		
M	1450	3	3·938	3·8 ± 0·8
C	1600	3	3·947	14·1 ± 1·5
Material	*Hot-pressing condition*		*Bulk density* ($g\ cm^{-3}$)	*Mean grain size* (μm)
	Temp. (°C)	*Pressure* (*MPa*)		
F	1300	20	3·89	1·2 ± 0·5

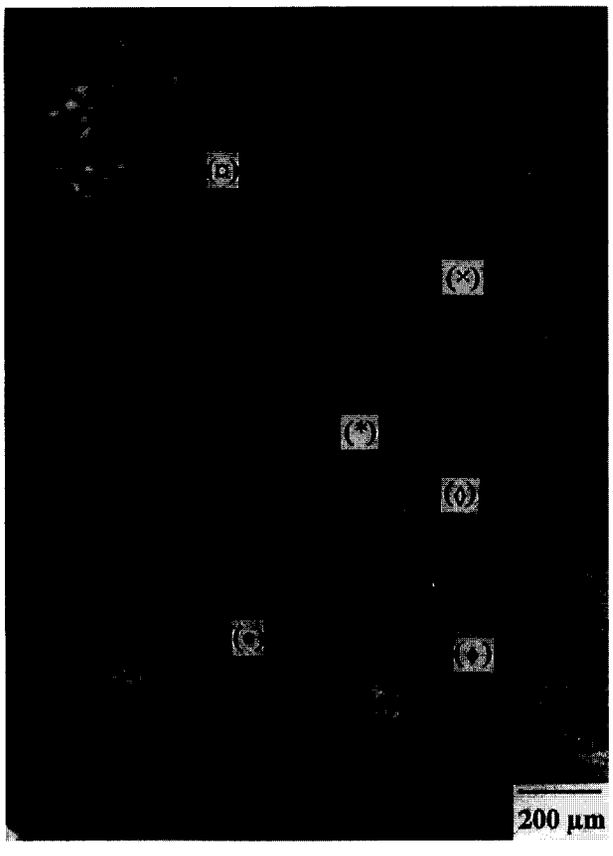

(a)

(b)

Fig. 7 Optical micrographs (Nomarski interference contrast). (a) Craters produced by slow indentation at loads of (×) 0·5 N, (*) 1 N, (◇) 2 N, (◆) 3 N, (●) 5 N and (○) 10 N and (b) craters produced by normal particle impacts at 180 rev min^{-1}.

$$R = -\frac{\Delta w}{A_{\text{imp}}\rho\Delta t} \tag{9}$$

where $\Delta w = w - w_0$. w_0 is the specimen weight before testing (t_0) and w is the specimen weight after testing for a time t. A_{imp} is the impacting area (worn area) and ρ is the specimen density.

4 Wet Erosive Wear Results of Polycrystalline Alumina and Sapphire Specimens

Figure 8 shows worn surfaces of polycrystalline alumina, mean grain size G = 1·2, 3·8 and 14·1 μm, and sapphire specimens, due to normal particle impacts at ~2·7 m s^{-1}(180 rev min^{-1}) for 660 min. The frontal view of the worn area for each specimen is shown in Fig. 8(a). For the same worn area the greatest amount of material removed is for the coarse-grained specimen, and this decreases as the grain size of the specimens becomes finer. This is more evident in the lateral views of the worn area as shown in Fig. 8(b). Notice that for all specimens the area exposed to impacts is the same although the damage depth varies.

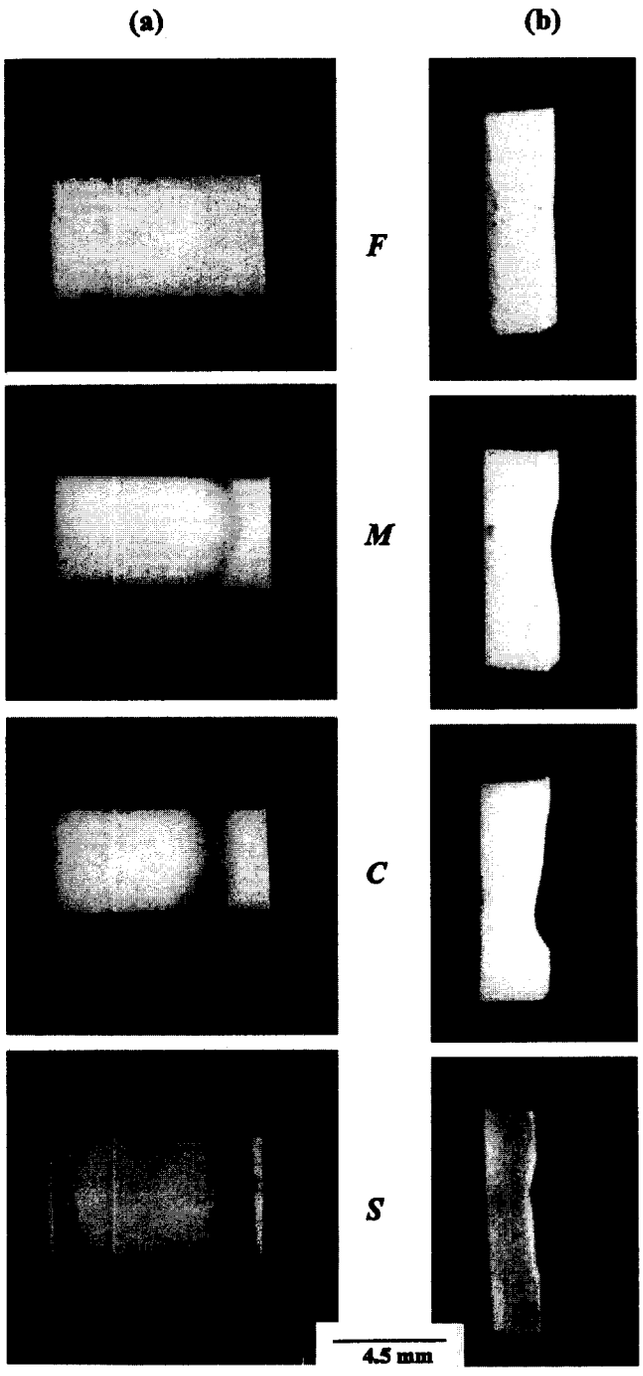

Fig. 8. (a) Frontal and (b) lateral views of the eroded surfaces of polycrystalline alumina [grain sizes 1·2 (F), 3·8 (M) and 14·1 μm (C)] and sapphire (S) specimens. Erosion rate increases with grain size.

Scanning electron micrographs of worn surfaces of polycrystalline alumina, G = 1·2, 3·8 and 14·1 μm, and sapphire specimens due to tests run for 1, 15 and 660 min at 2·7 m s^{-1} impact speed (180 rev min^{-1}) are shown in Figs 9, 10 and 11, respectively. In tests run for a short period of time (Fig. 9), single particle impacts produce clusters of damage which may be isolated or linked to each other. Also, there is some plastic deformation similar to that produced by Vickers hardness indentation. At this early stage of damage it is already clear that the wear of the polycrystalline alumina specimens is grain-size-dependent. The damage evolution is clear for tests run for a longer period of time (Fig. 10), where loss of whole grains and transgranular fracture are already evident. At a later stage (Fig. 11) the damage is much more severe and grain loss and transgranular fracture are predominant. Notice that for the finest grain size specimen (G = 1·2 μm) plastic deformation or polishing is always present.

The weight loss versus impacting time for each specimen is plotted in Fig. 12. The weight loss increases linearly with time. The weight loss of polycrystalline alumina specimens increases with the grain size.

Figure 13(a) shows the wear rate for polycrystalline alumina and sapphire specimens calculated using eqn (9). The worn area was measured directly on the specimens and was the same for all specimens, 3·32 × 10^{-5} m^2. The density for polycrystalline specimens was taken as in Table 3, and for the single crystal specimen as 3·98 g cm^{-3}. The coarse-grained specimen, C, exhibited a wear rate about one order of magnitude higher than that of the finest grain size specimen, F. For the sapphire specimen, S, the wear rate was intermediate between those of the medium grain (M) and coarse grain (C) specimens.

The wear rates due to normal particle impacts presented here are apparently about 10 times lower than the results presented by Miranda-Martinez *et al.*[9], Table 4, for specimens of the same grain size and sintered under the same conditions. However, the two experimental methods used vary in the following respects.

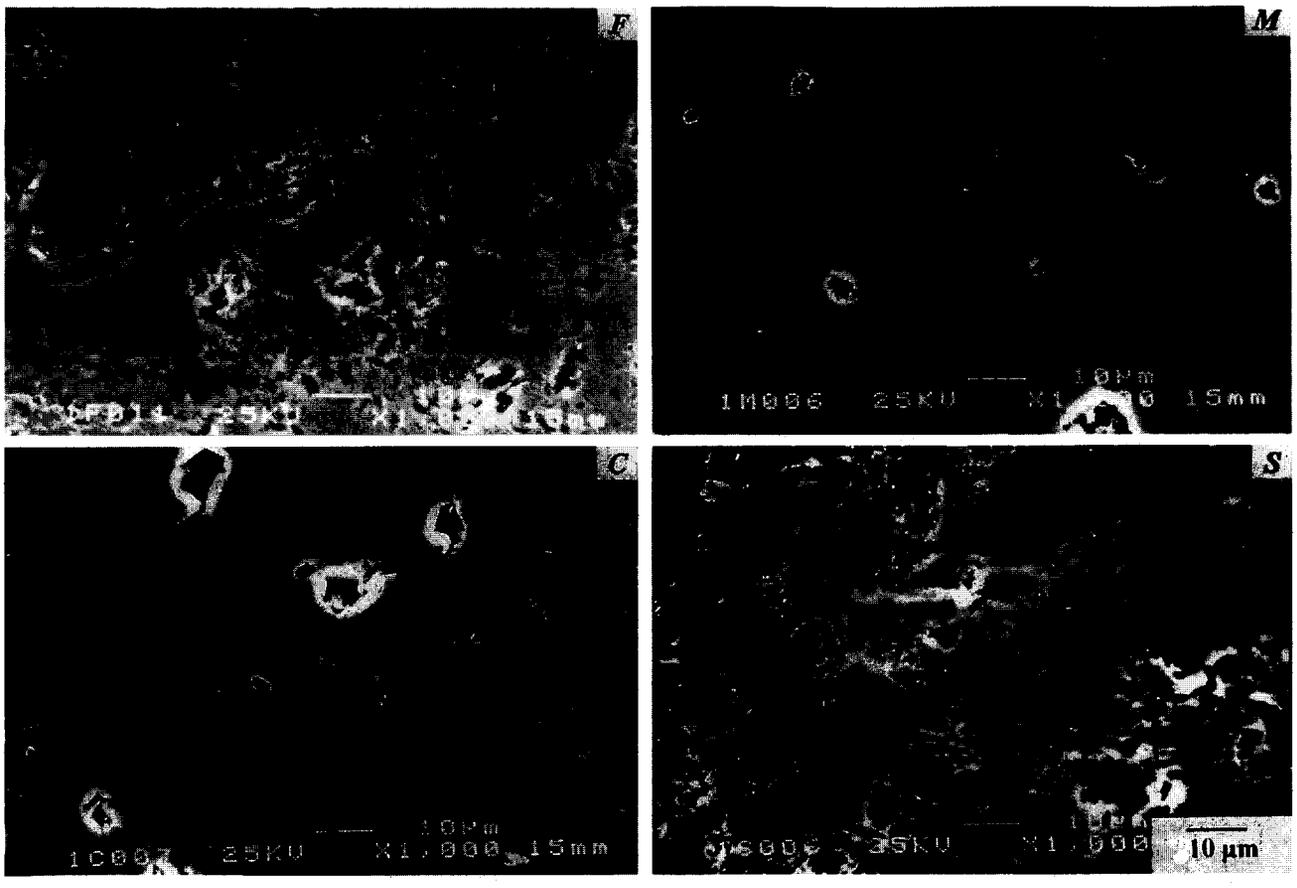

Fig. 9. Scanning electron micrographs of eroded surfaces of polycrystalline alumina [grain sizes 1·2 (F), 3·8 (M) and 14·1 μm (C)] and sapphire (S) specimens. Test time: 1 min.

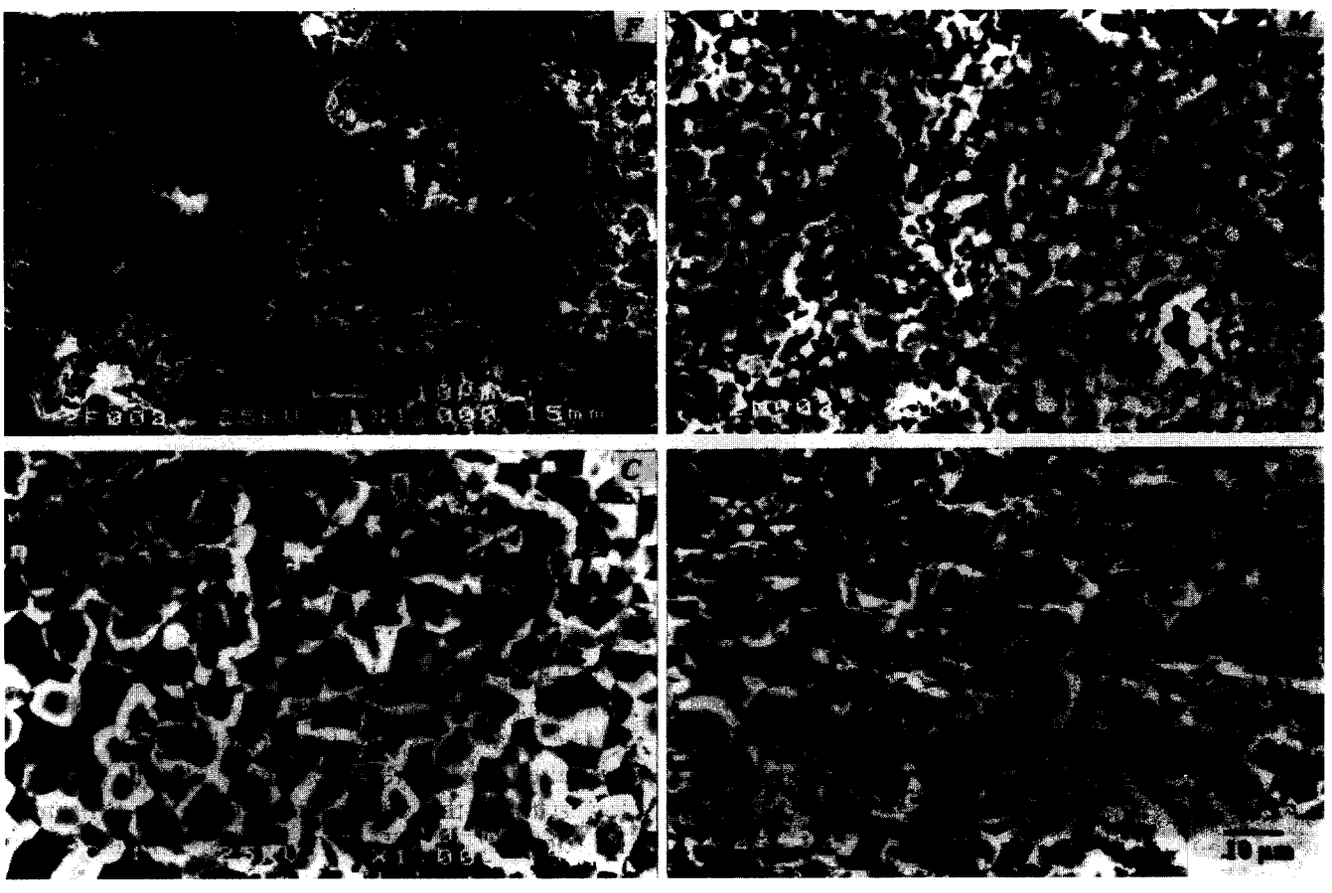

Fig. 10. Scanning electron micrographs of eroded surfaces of polycrystalline alumina [grain sizes 1·2 (F), 3·8 (M) and 14·1 μm (C)] and sapphire (S) specimens. Test time: 15 min.

(1) The particle flux — in our experiments this is $8{\cdot}6 \times 10^7$ particles m^{-2} s^{-1}; for Ref. 9 we estimate (using data from Riley[20]) a flux of $1{\cdot}92 \times 10^9$ particles m^{-2} s^{-1}. In Fig. 13(b) and Table 4, results are shown normalized to the same flux, as erosion rate per impacting particle. The erosion rates from Ref. 9 are then approximately four times lower per particle than in our results.
(2) The velocity of impact — this is ~2·7 m s^{-1} in our experiments, ~1·9 m s^{-1} in those of Ref. 9. Lower impact velocities would be expected to give lower erosion rates.
(3) The angle of incidence of the particles — in our experiments this is always 90°; in those of Ref. 9 the angle is not controlled and probably ranges from 0 to 90°. For ceramic materials, the erosion rate decreases markedly as the impact angle decreases from 90°.

Both the last two factors will tend to give lower erosion rates per impacting particle for the results of Miranda-Martinez *et al.*[9] as observed.

5 Conclusions

A new apparatus to study the erosive wear mechanism of brittle materials due to normal particle impacts has been designed and constructed. The apparatus consists of a jet body (funnel–nozzle) which rotates immersed in a slurry medium in a pot.

The velocity of particle impacts was determined by a model [eqn (8)] based on the balance between the kinetic energy of a spherical particle and the work of slow load indentation of a spherical indenter to produce the same plastic deformation in soft materials. The model enables us to calculate the normal impact velocity solely as a function of the crater depth produced by impacts.

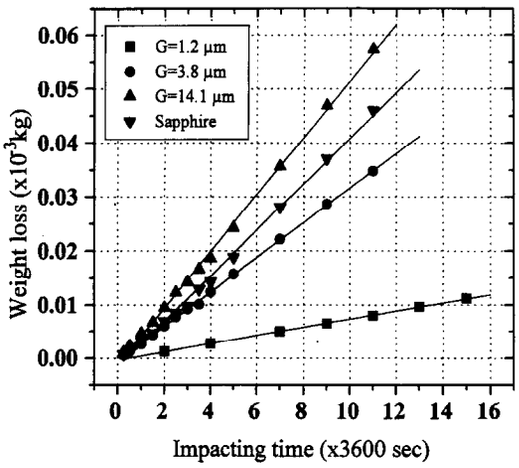

Fig. 12. Weight loss versus impacting time. The weight loss increases linearly with test duration, and depends strongly on grain size.

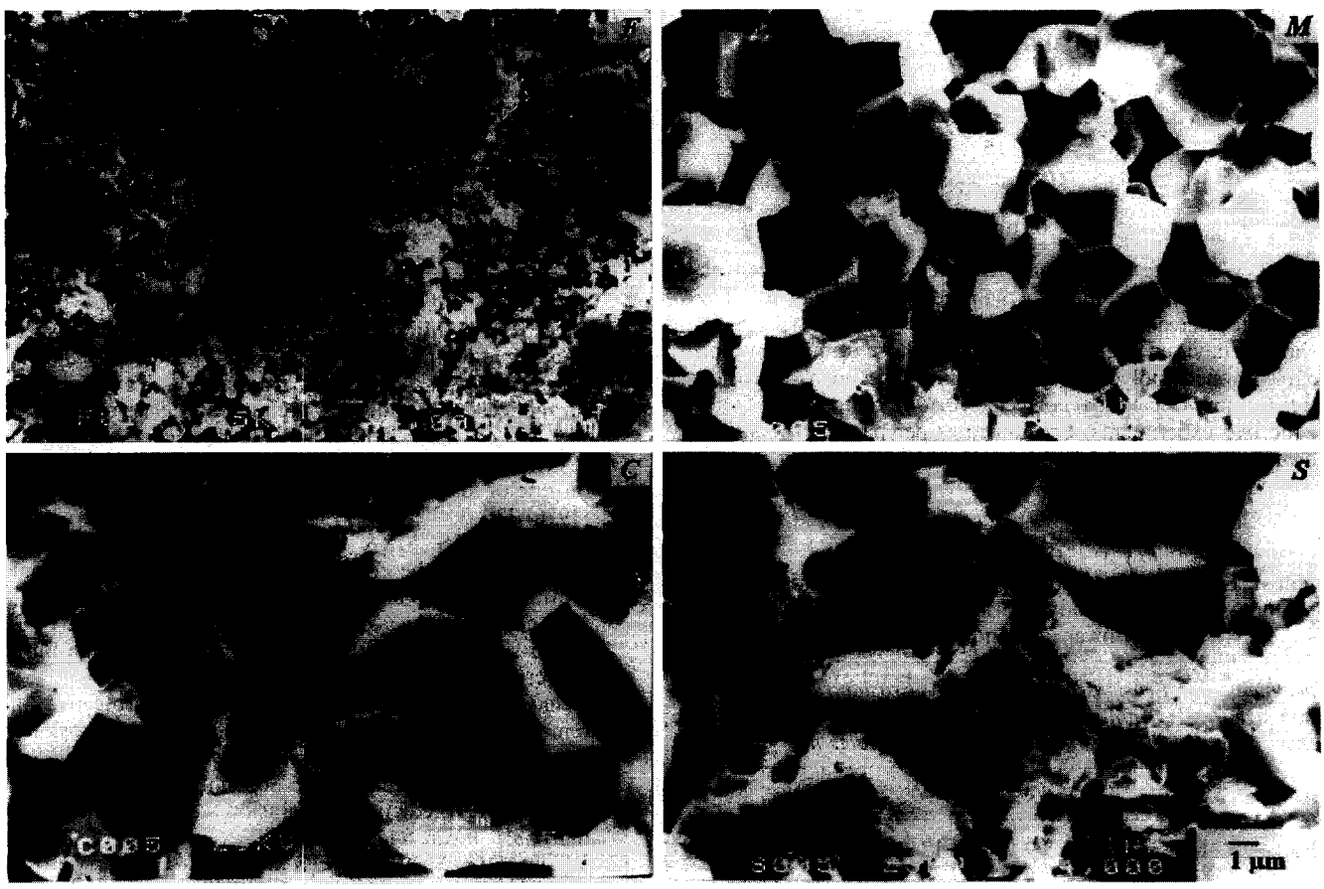

Fig. 11. Scanning electron micrographs of eroded surfaces of polycrystalline alumina [grain sizes 1·2 (F), 3·8 (M) and 14·1 μm (C)] and sapphire (S) specimens. Test time: 660 min.

Worn surfaces of polycrystalline alumina specimens produced by normal particle impacts at ~2·7 m s^{-1} for test times of 1, 15 and 660 min were studied. The wear mechanism at the early stage of damage is similar to that at a later stage where severe damage has taken place.

Weight loss of polycrystalline alumina and sapphire specimens due to normal particle impacts of SiC grits in water increased linearly with impacting time.

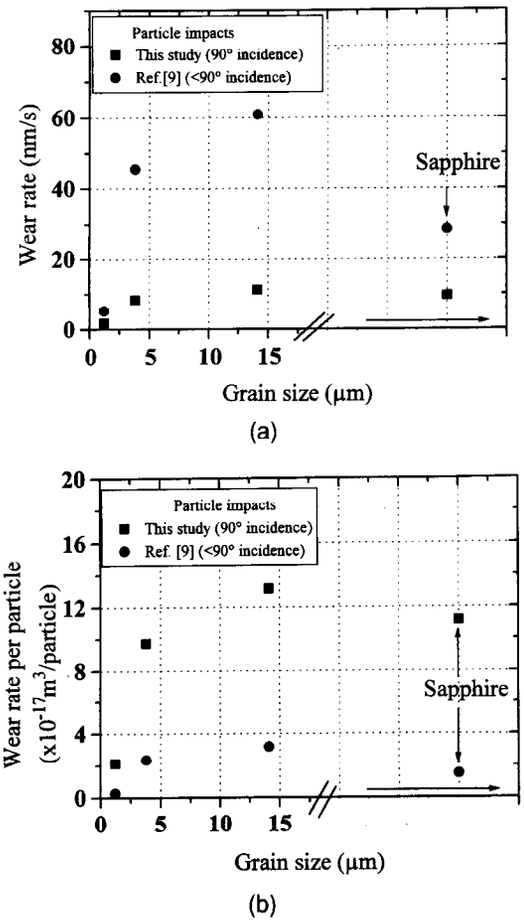

Fig. 13. Wear rate versus grain size for normal incidence (this study) and from the study of Miranda-Martinez *et al.*[9] The wear rate increases with grain size and sapphire specimens exhibit behaviour intermediate between those of medium- and coarse-grained polycrystalline alumina specimens. Erosion rates (a) uncorrected, (b) corrected for different particle fluxes in the two experiments. Erosion rates per particle (b) due to normal impacts are higher than those due to lower impact angles.[9]

Table 4. Erosion rate of polycrystalline alumina and sapphire specimens, from this study (normal impacts, 90°) and from Ref. 9 (lower incidence angles. <90°)

Specimen grain size (*μm*)	*Erosion rate* (*nm* s^{-1}) *Impacts at*		*Erosion rate* (*10^{-17} m^3 per particle*) *Impacts at*	
	90°	*<90°*	*90°*	*<90°*
1·2	1·83 ± 0·7	5·9	2·12 ± 0·08	0·27
3·8	8·36 ± 0·8	45·6	9·72 ± 0·09	2·37
14·1	11·30 ± 0·6	61·0	13·14 ± 0·06	3·18
Sapphire	9·56 ± 0·6	28·6	11·20 ± 0·08	1·48

The measured wear rate of polycrystalline alumina specimens is grain-size-dependent, being about one order of magnitude greater for Al_2O_3 of 14·1 μm grain size than for 1·2 μm grain size. For sapphire, the wear rate is between those of the medium and coarse grain size polycrystalline alumina specimens.

The erosion rates per impacting particle from our study are about four to 10 times higher than those of Miranda-Martinez *et al.*,[9] which we attribute to the effects of impacting angle[30] and particle velocity on erosion rate.

Acknowledgements

A. Franco thanks CAPES (Brazilian Government) for financial support. This work was also supported by the EPSRC under Grant No. J86513. We thank F. L. Riley, R. W. Davidge and P. Twigg for assistance with specimen preparation, provision of data in advance of publication, and for many useful discussions. Many thanks to J. Short for assistance with the construction of the machine, and to A. McKnight for photographic assistance.

References

1. Wu, C. Cm., Rice, R. W., Johnson, D. & Platt B. A., Grain size dependence of wear in ceramics. *Ceram. Eng. Sci. Proc.*, **6** [7–8] (1985) 995–1011.
2. Cho, S.-J., Hockey, B. J., Lawn, B. R. & Bennison, S. J., Grain-size and R-curve effects in the abrasive wear of alumina. *J. Am. Ceram. Soc.*, **72** (1989) 1249–52.
3. Deckman, D. E., Jahanmir, S. & Hsu, S. M., Wear mechanisms of α-alumina lubricated with a paraffin oil. *Wear*, **149** (1991) 155–68.
4. Liu, H. & Fine, M. E., Modelling of grain-size dependent microfracture-controlled sliding wear in polycrystalline alumina. *J. Am. Ceram. Soc.*, **76** (1993) 2393–6.
5. Rice, R. W., Micromechanics of microstructural aspects of ceramic wear. *Ceram. Eng. Sci. Proc.*, **6** (1985) 940–58.
6. Marshall, D. B., Lawn, B. R. & Cook, R. F., Microstructural effects on grinding of alumina and glass ceramics. *J. Am. Ceram. Soc.*, **70** (1987) C-139–40.
7. Rice, R. W. & Speronello, B. K., Effect of microstructure on rate of machining of ceramics. *J. Am. Ceram. Soc.*, **59** (1976) 330–3.
8. Wiederhorn, S. M. & Hockey, B. J., Effect of material parameters on the erosion resistance of brittle materials. *J. Mater. Sci.*, **18** (1983) 766–89.
9. Miranda-Martinez, M., Davidge, R. W. & Riley, F. L., Grain size effects on the wet erosive wear of high-purity polycrystalline alumina. *Wear*, **172** (1994) 41–8.
10. Zahavi, J. & Wagner, H. J., The role of protective film removal and growth on the rate of erosion-corrosion in metals. *Proc. 5th Int. Conf. on Erosion by Liquid and Solid Impact*, Cambridge, UK, 3–6 September 1979, Paper 50.
11. Elkholy, A., Prediction of abrasion wear for slurry pump materials. *Wear*, **84** (1983) 39–49.
12. Wright, I. G., Shetty, D. K. & Clauer, A. H., Slurry erosion of WC–Co cermets and its relationship to materials properties. *Proc. 6th Int. Conf. on Erosion by Liquid and Solid Impact*, Cambridge, UK, 5–8 September 1983, Paper 63.

13. Sagüés, A. A., Spencer, D. K., Sethi, V. K. & Sargent G. A., Slurry erosion and abrasion of metal-ceramic coatings. In *Slurry Erosion, Uses, Applications, and Test Methods* eds J. E. Miller & F. E. Schmidt, Jr. ASTM STP 946, American Society for Testing and Materials, Philadelphia, PA, 1987, pp. 19–44.
14. Matsumura, M., Oka, Y. & Yamawaki, M., Slurry erosion–corrosion of commercially pure iron in fountain-jet testing facility—mechanism of erosion. *Proc. 7th Int. Conf. on Erosion by Liquid and Solid Impact*, Cambridge, UK, 7–10 September 1987, Paper 40.
15. Zu, J. B., Hutchings, I. M. & Burstein, G. T., Design of a slurry erosion test rig. *Wear*, **140** (1990) 331–44.
16. Lee, Y. H. & Clark, H. McI., The relative erosion of coal–oil, coal–water, and petroleum coke–oil slurries. In *Slurry Erosion, Uses, Applications and Test Methods*, eds J. E. Miller & F. E. Schmidt, Jr. ASTM STP 946, American Society for Testing and Materials, Philadelphia, PA, 1987, pp. 44–61.
17. Tsai, W., Humphrey, J. A. C., Cornet, I. & Levy, A. V., Experimental measurement of accelerated erosion in a slurry pot tester. *Wear*, **68** (1981) 289–303.
18. de Bree, S. E. M., Rosenbrand, W. F. & de Gee, A. W. J., On the erosion resistance in water–sand mixtures of steels for application in slurry pipelines. *Proc. 8th Int. Conf. on the Hydraulic Transport of Solid in Pipes*, Johannesburg, 25–27 August 1982. BRHA Fluid Eng., Cranfield, Bedfordshire, 1982, Paper C3.
19. Schumacher, W. J., Ball mill and hub test methods for slurry erosion evaluation of materials. In *Slurry Erosion, Uses, Applications and Test Methods*, eds J. E. Miller & F. E. Schmidt, Jr. ASTM STP 946, American Society for Testing and Materials, Philadelphia, PA, 1987, pp. 5–18.
20. Clark, H. McI., On the impact rate and impact energy of particles in slurry pot erosion tester. *Wear*, **147** (1991) 165–83.
21. Hutchings, I. M., A model for erosion of metals by spherical particles at normal incidence. *Wear*, **70** (1981) 269–81.
22. Kosel, T. H., Anand, K., Sundararaman, V., Sriram, T. S., Kotteyil, M. & Nailos, P. J., Rebound of erodent particles from metal surfaces. In *Corrosion–Erosion–Wear of Materials at Elevated Temperatures*, ed. A. V. Levy. NACE, 1991, pp. 8–1–8–28.
23. Tabor, D., *The Hardness of Metals*. Clarendon Press, Oxford, 1951.
24. Hutchings, I. M., Strain rate effects in microparticle impact. *J. Phys. D*, **10** (1977) L179–84.
25. Clark, H. McI., A comparison of particle impact in gas–solid and liquid–solid erosion. In *ELSI VIII, Proc. 8th Int. Conf. on Erosion by Liquid and Solid Impact*, eds I. M. Hutchings & J. A. Little. Cambridge, UK, 4–8 September 1994, pp. 465–72.
26. Kosel, T. H., Private communication, University of Notre Dame, 1992.
27. Tabor, D., Collisions through liquid layers. *Engineering*, **167** (1949) 145–7.
28. Wong, K. K. & Clark, H. McI., A model of particle velocities and trajectories in a slurry pot erosion test. *Wear*, **160** (1993) 95–104.
29. Riley, F. L., Private communication, University of Leeds, 1995.
30. Finnie, I., Erosion of surfaces by solid particles. *Wear*, **3** (1960) 87–103.